

TREVR: A general $O(N \log^2 N)$ radiative transfer algorithm

J. J. Grond, R. M. Woods, J. Wadsley [★] and H. M. P. Couchman

Department of Physics and Astronomy, McMaster University, Hamilton, Ontario L8S 4M1, Canada

Accepted XXX. Received YYY; in original form ZZZ

ABSTRACT

We present TREVR (Tree-based Reverse Ray Tracing), a general algorithm for computing the radiation field in astrophysical simulations. TREVR prioritizes the ability to handle large numbers of sources and computational speed whilst maintaining a specified level of accuracy via adaptive refinement. TREVR is based on a *tree* data structure similar to many gravity and hydrodynamics solvers. This allows for computation of the radiation field in $O(N \log N_{\text{source}})$ time without absorption and $O(N \log N_{\text{source}} \log N)$ time with absorption. This scaling is made possible by merging sources of radiation according to an opening angle criteria and walking the tree structure to trace a ray. The computational complexity we quote accounts for the use of adaptive refinement, a main feature that is unique to TREVR among other radiative transfer methods. We provide a suite of tests demonstrating the algorithm’s ability to accurately compute fluxes, ionization fronts and shadows. We also analyze the algorithm’s computational complexity, in how it scales with the number of sources and sinks. Further examinations of how the aforementioned refinement criterion’s value affects computational cost and accuracy are presented. Finally, we discuss strengths and shortcomings of this algorithm, how they constrain the types of problems TREVR can handle and how these shortcomings can be remedied if possible.

Key words: radiative transfer – methods: numerical

1 INTRODUCTION

Radiation is arguably the most important physical phenomena to the field of astrophysics. Almost all of the information we receive from outer space comes in the form of photons we detect on or around earth. Understanding the process of radiative transfer (RT) is key in interpreting this information, as the photons are affected by the medium they travel through on their way to our telescopes and detectors. Interactions between photons and the medium do not only affect the photons themselves but the matter as well. Photons and baryons exchange energy and momentum, affect the excitation and ionization states of said baryons and thus determine the chemical and thermodynamic properties of the bulk medium. This in turn makes radiation a driving factor in many of the astrophysical processes we study.

On galaxy scales, the question of how feedback mechanisms affect star and galaxy formation is one of these physical processes we can study. Stellar feedback comes in the form of photoionization by ultraviolet (UV) radiation, stellar winds and supernovae (Leitherer et al. 1999), the latter of which has been a main focus in simulations in previous years Grond: cite a bunch of SN feedback papers?.

It is important to note that even though supernovae might be spectacularly powerful events, ionizing radiative output from stellar populations in the UV regime contributes two orders of magnitude more power at early times and about 50 times more energy over the course of a stellar population’s lifetime. This is made evident in Figure 1, a plot of luminosity output per solar mass as a function of time from stellar populations created via output from the stellar evolution code Starburst99 (Leitherer et al. 1999).

However, the way in which this massive output of UV radiation is deposited and consequently affects the interstellar medium (ISM) is still unclear. Attempts at numerically exploring these affects without the use of a full radiative transfer method have produced conflicting results. Simulations done by Gritschneider et al. (2009) and (Walch et al. 2012) suggest that ionizing feed back from large O-type stars before the first supernovae ($< 1 - 3\text{Myr}$) have a significant effect on star formation rate. Whereas Dale et al. (2012) conclude the affects on star formation rate to be small.

With that in mind it may then come as a surprise that RT has been treated rather poorly in most large scale astrophysical simulations, usually as some imposed uniform background. This is not because of carelessness or lack of effort, but because RT is an intrinsically complex and expensive problem. The complexity of this problem is firstly

[★] E-mail: wadsley@mcmaster.ca

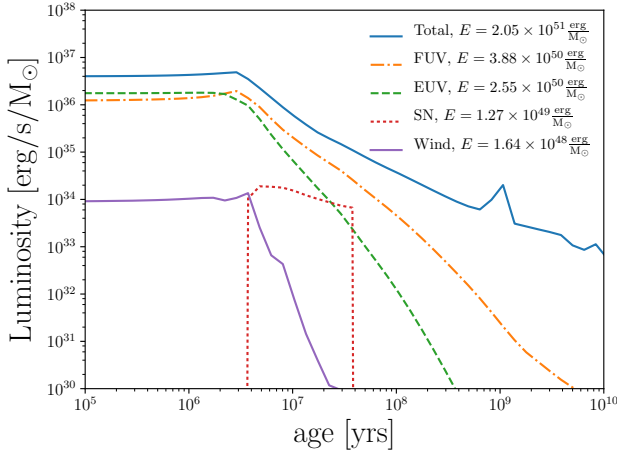


Figure 1. Luminosity per solar mass as a function of time for a stellar population having a Chabrier initial mass function (Chabrier 2003).

evident in the classical RT equation (e.g. Mihalas & Mihalas 1984),

$$\left[\frac{1}{c} \frac{\partial}{\partial t} + \hat{\mathbf{n}} \cdot \nabla \right] I(\mathbf{x}, \hat{\mathbf{n}}, t, \nu) = \epsilon(\mathbf{x}, \hat{\mathbf{n}}, t, \nu) - \alpha(\mathbf{x}, \hat{\mathbf{n}}, t, \nu) I(\mathbf{x}, \hat{\mathbf{n}}, t, \nu), \quad (1)$$

where I , ϵ and α are the intensity, emissivity and extinction coefficients respectively and all depend on position \mathbf{x} , unit direction of light propagation $\hat{\mathbf{n}}$, time t and frequency ν . Apart from being a seven dimensional problem, RT has the highest possible characteristic speed of c , the speed of light. Also, unlike a force at a distance problem such as gravity, RT depends on the properties of the intervening material which is handled by the extinction term, α .

Because of this complexity, a naïve numerical solution to the RT problem scales with the number of resolution elements like $\mathcal{O}(N^{7/3})$ and requires a timestep thousands of times smaller than typical courant times in astrophysics. This costly scaling is simply a result of the three major parts that go into computing the radiation field in a simulation. Firstly, a radiation field is represented by a simulation’s N resolution elements, so the field intensity needs to be computed at N points in the simulation volume. Secondly, each resolution element’s intensity value is made up of contributions from N_{source} sources of radiation. This can also be thought of as N_{source} rays of light being computed per resolution element. This leads to a scaling for the total number of rays computed in a simulation going as $N_{\text{ray}} = N \times N_{\text{source}}$, which is $\mathcal{O}(N^2)$ assuming the $N_{\text{source}} = N$. This fact alone limits rudimentary RT methods to only small scale problems, such as ionization by a small handful of massive stars (Howard et al. 2016, 2017), to avoid $\mathcal{O}(N^2)$ scaling. Finally, each ray of light interacts with the medium along its path as mentioned earlier. Since the medium is represented by the simulation’s N resolution elements and N is proportional to the simulation volume, a one dimensional ray intersects with $\mathcal{O}(N^{1/3})$ resolution elements. Using the total number of resolution elements interacted with as a measure of computational cost we get that the computational cost is proportional to $N \times N_{\text{source}} \times N^{1/3}$, which is $\mathcal{O}(N^{7/3})$. This poor

scaling with resolution elements makes it unfeasible to simulate RT along with gravity and hydrodynamics methods that scale like $\mathcal{O}(N \log N)$. After breaking down the source of computational complexity in the RT problem it is evident that something needs to be done about the strong dependence on N_{source} and the $N^{1/3}$ cost of computing each ray to attain a feasible RT method.

A feasible RT method would have to solve a simplified RT problem. The first one of these simplifications divides RT methods into two different categories based on how they treat c in Eq. 1. For methods that use a finite c , which is often a reduced speed of light, the partial time derivative remains in Eq. 1 and the radiation field is advected or “evolved”. Methods that solve the RT equation in this way, which we will call evolutionary methods, include moment methods like OTVET (Gnedin & Abel 2001) and RAMESE-RT (Rosdahl & Teyssier 2015) as well as photon packet propagation methods like TRAPHIC (Pawlik & Schaye 2008), SPHray (Altay et al. 2008) and SimpleX2 (Paardekooper et al. 2010). On the other hand, in limit where c is taken to be infinite, the partial time derivative in Eq. 1 goes to zero and the radiation field can be computed instantaneously as a computational geometry problem. Methods that solve the RT equation in this way, which we will refer to as instantaneous methods, include forward ray tracers such as C²Ray (Mellema et al. 2006), Moray (Wise & Abel 2011) and Fer-vent (Baczynski et al. 2015) as well as reverse ray tracers such as TreeCol (Clark et al. 2012) and URCHIN (Altay & Theuns 2013).

Instantaneous methods typically take the form of ray tracers. Ray tracers are the most simple, natural way to go about solving the RT problem. Forward ray tracers trace many rays outward from sources of radiation, similarly to the actual phenomena, in hope that they will intersect resolution elements for which the radiation field will be computed. As a result, a number of rays per source comparable to the number of resolution elements is needed to insure accuracy. Thus, naïve ray tracers scale with number of resolution elements like $\mathcal{O}(N N_{\text{source}} N^{1/3})$. This scaling limits forward ray tracers to problems with few sources to avoid $\mathcal{O}(N^{7/3})$ like scaling. **Wadsley: Note the bit about ray clumping not really saving the day because you still end up with $\mathcal{O}(N)$ ray segments and often a large multiplier (e.g. Abel & Gnedin approach). Grond: Need some clarification on this point.**

Recently there has been some focus on reverse ray tracing methods by Clark et al. (2012) and Altay & Theuns (2013). These methods are not general, as they specifically compute continuum radiation (from the post ionization UV background) and not from internal sources of radiation. However, the idea of reverse ray-tracing introduces many advantages relative to reverse raytracing. A main difference between forward and reverse ray tracing is that reverse ray tracers trace rays from the resolution elements directly to the sources of radiation. Tracing from the sinks guarantees the density distribution is well sampled near the resolution element as apposed to forward ray tracing where one would have to increase the number of rays per sink to guarantee this type of accuracy. Put simply, radiation is computed exactly where it is needed. This is especially advantageous in adaptive mesh and Lagrangian simulations such as smoothed

particle hydrodynamics (SPH) simulations, as low density regions are represented by few resolution elements, and thus extra work is not done to resolve said regions. An added benefit to reverse ray tracing that adaptive time steps can be used. However, just performing a naïve reverse ray trace does not avoid $O(NN_{\text{source}}N^{1/3})$ scaling with resolution elements, and so the inability to model many sources remains the most significant barrier current instantaneous methods face when trying to solve the general RT problem. However, on any given substep N_{sink} can be dramatically reduced to be just the active sinks. In simulations with adaptive timesteps the active fraction on a given step is typically less than a percent of the total.

Evolutionary methods are typically based on evolving moments of the radiation field stored at each resolution element. They have no dependence on the number of sources, and scale like $O(N)$ with the number of resolution elements, allowing them to handle large numbers of sources and scattering. Although evolutionary methods can handle both optically thin and thick regimes, they lose directional accuracy in intermediate regimes and suffer from directional accuracy in general.

Photon packet propagation methods, such as TRAPHIC (Pawlik & Schaye 2008), are an evolutionary approach that performs better in the optically thin regime. TRAPHIC introduces virtual particles (ViPs) to propagate their photon packets in less dense, optically thin regions lacking in SPH particles. They also preserve directionality quite well, however Monte Carlo aspects of how they propagate their photon packets introduce significant Poisson noise into their computed radiation field. Monte Carlo resampling is shown to reduce this noise but is quite expensive and deteriorates the initially sharp shadows. Both of these methods scale linearly with resolution elements as mentioned before, but are also forced to operate on every resolution element. In moment methods the radiation field for every grid cell needs to be computed, and in photon packet propagation methods the photon packets hop particle to particle. In the case of TRAPHIC, their N is even greater than the number of SPH particles including the addition of ViPs. **Wadsley: Need to discuss timestepping for evolutionary methods. Grond: Need some clarification.** Regardless, TRAPHIC is arguably the best general RT method due to its ability to handle both the optically thick and thin regimes with feasible scaling.

We hope from this introduction to the state of the art in RT methods it is apparent that there is room for improvement, especially in the area of instantaneous methods. Although promising work has been done with reverse ray tracers like TreeCol and URCHIN, a general implementation of one has yet to be developed and published. There is also the problem of scaling with radiation sources in instantaneous methods that reverse ray tracers alone do not solve. Therefore we have developed TREVR, a $O(N \log^2 N)$ reverse ray tracer designed to solve these problems and fill this niche. In Section 2 we detail the specific RT equations TREVR solves (Subsection 2.1) and the general TREVR algorithm (Subsection 2.2) as well as specifics of our implementation in GASOLINE (Subsection 2.3). In Section 3 we present a suite of tests demonstrating the algorithm's ability to accurately compute fluxes, ionization fronts and shadows

in the optically thick and thin regimes. These tests also allow us to explore how TREVR's accuracy criteria predicts error and affects computation cost. The computational cost is bounded and characterized in a general case to substantiate the $O(N \log^2 N)$ claim made earlier. Finally, in Section 4 we discuss TREVR's strengths and shortcomings and conclude how they enable and constrain the types of problems TREVR can handle. We will also discuss apparent improvements that can be made in the future in this section.

2 METHOD

2.1 Simplifications to the full RT problem

Before describing TREVR, let's first define the simplified version of the classical RT equation the method solves. Since TREVR is an instantaneous method, c is set to infinity eliminating the partial time derivative in 1 leaving us with the instantaneous RT equation,

$$\hat{\mathbf{n}} \cdot \nabla I(\mathbf{x}, \hat{\mathbf{n}}, t, \nu) = \epsilon(\mathbf{x}, \hat{\mathbf{n}}, t, \nu) - \alpha(\mathbf{x}, \hat{\mathbf{n}}, t, \nu) I(\mathbf{x}, \hat{\mathbf{n}}, t, \nu). \quad (2)$$

The emissivity term in the above equation, ϵ , describes a continuous emitting medium. TREVR assumes sources of radiation are continuous, but being a numerical method it needs to represent sources of radiation as discrete resolution elements. In this case ϵ is a sum of delta functions and the solution to the RT equation becomes a linear combination of contributions from all sources of radiation. Also, since we are considering sources one by one we can start using the path length s between a source and resolution element as our integration element

$$\frac{dI}{ds} = -\alpha I. \quad (3)$$

We can then combine the path length and extinction coefficient to solve for intensity by integrating

$$d\tau = \kappa \rho ds, \quad (4)$$

the optical depth, where κ is opacity and ρ is density. This leaves us with

$$\frac{dI}{d\tau} = -I, \quad (5)$$

the final version of the RT problem this method solves. The solution to this equation is

$$I(s) = I(s_0)e^{-\tau(s)}, \quad (6)$$

where $I(s_0)$ is the intensity of the source and $\tau(s)$ is the only quantity to be integrated in our method

$$\tau(s) = \int_{s_0}^s \kappa(s) \rho(s) ds. \quad (7)$$

Wadsley: This is a bit out of the blue. You just skipped from one source to all of them without saying you did that. Grond: I'm a bit stuck on this.

We can use the radiation intensity directly in heating, chemistry and ionization functions which are typically a function the total intensity from all radiation sources. We can then take moments of the intensity to obtain useful quantities such as radiation flux

$$\mathbf{F} = \int I \cos \theta d\Omega \hat{\mathbf{n}}, \quad (8)$$

and radiation pressure

$$\mathbf{p} = \frac{1}{c} \int I \cos^2 \theta d\Omega \hat{\mathbf{n}}. \quad (9)$$

Wadsley: What is dOmega – where did the integrals come from? Grond: Rybicki and Lightman. Wadsley: It might be clearer if you said, “for point sources the contribution is I delta(theta)” or something like that. Grond: Need some clarification here. Because we assume our sources of radiation to be true point sources, $\cos \theta = 1$. If the angular size of a resolution element relative to the source of radiation is small enough such that the small angle approximation holds true, it should also hold that there is a one-to-one correspondence between intensity and flux. Thus, flux from a *single* source can be written simply as

$$\mathbf{F} = I(s_0) e^{-\tau(s)} \hat{\mathbf{n}} = \frac{L}{4\pi s^2} e^{-\tau(s)} \hat{\mathbf{n}}, \quad (10)$$

where L is the luminosity of the source of radiation. The total flux is then computed by summing up flux contributions from all sources. For the remainder of paper we represent the radiation field as flux values computed via the above expression.

2.2 Algorithm

Please note that although TREVR has been initially implemented in the SPH code GASOLINE (Wadsley et al. 2004), TREVR is not specific to GASOLINE or SPH in general. The method only requires that the simulation volume is hierarchically partitioned in space and so it could be used directly in an adaptive mesh refinement (AMR) code.

The TREVR algorithm is based around a tree data structure which partitions the simulation volume hierarchically in space. The smallest resolution elements are or are contained by in the leaf nodes of the tree data structure. In Lagrangian or “particle” methods such as SPH, a number of SPH particles can be contained by a leaf node or “bucket”. The maximum number of particles per bucket is referred to as N_B . In Eulerian or “grid” based methods the bucket is the smallest grid cell itself, so N_B is effectively one. N resolution elements hold radiation intensity values and represent the radiation field TREVR computes.

2.2.1 Source Merging

As mentioned in the introduction, a naïve algorithm would compute interactions between a resolution element and all sources of radiation. If we assume the number of resolution elements is equal to the number of sources, an infeasible number of interactions would need to be computed, scaling like $O(N^2)$. To mitigate this N^2 scaling TREVR employs source merging similar to particle merging in the Barnes & Hut (1986) tree-based gravity solver which has remained commonplace in astrophysical simulations (Benz 1988; Vine & Sigurdsson 1998; Springel et al. 2001; Wadsley et al. 2004; Hubber et al. 2011). Merging sources of radiation was first implemented in a rudimentary version of TREVR that did not consider extinction of any kind (Kannan et al. 2014). Sources of radiation are merged together at their centre of

luminosity if they meet an “opening angle” criteria. This criteria is defined as

$$\theta_{\text{open}} > l/r, \quad (11)$$

where l is the side length of a tree cell, r is the distance between the centre of luminosity of a source and centre of mass of a resolution element and θ_{open} is the opening angle, a fixed accuracy parameter. If a group of sources occupy the biggest tree cell that meets this criteria, all sources in that cell are merged into one, considerably reducing the number of interactions TREVR computes. This is illustrated in the left panel of Fig. 2, where the grey angle represents a cell whose angular size meets the opening angle criterion.

The cost savings of source merging can be quantified by integrating the number of tree cells that are “opened” according to the opening angle criteria. These opened cells will have their sources merged making them a single source. We will call the total count of the opened cells N_{open} . We can theoretically compute N_{open} this by integrating spherical shells of thickness dr along the path from a resolution element r , and then dividing the sphere volume by the volume of an opened cell, $V_{\text{open}}(r)$.

$$N_{\text{open}} = \int_{R_0}^R \frac{4\pi r^2}{V_{\text{open}}(r)} dr \quad (12)$$

The bounds of the above integral go from R_0 , the size of a bucket cell, to R , the length of the simulation volume. Because the number of particles in a simulation is proportional to the simulation volume, the lower integration limit can be expressed using particle numbers via

$$\frac{R_0}{R} = \sqrt[3]{\frac{N_B}{N}}, \quad (13)$$

the cubed root of the ratio of the average number of particles per bucket, N_B , to the total number of simulation particles. Note that N_B ($N_B = 10$ for this paper) is only needed for particle methods. In a grid method a bucket is just the lowest level grid cell in the tree and $N_B = 1$. The opened cell volume can also be rewritten by cubing the opening angle criteria

$$V_{\text{open}}(r) = l^3 = \theta_{\text{open}}^3 r^3. \quad (14)$$

Substituting gives us the following integral and its solution,

$$N_{\text{open}} = \int_{\left(\frac{N}{N_B}\right)^{-\frac{1}{3}}}^R \frac{4\pi r^2}{\theta_{\text{open}}^3 r^3} dr \sim \log N/N_B. \quad (15)$$

This result means that the number of interactions scales like $O(N \log N)$. This is also the total cost scaling in the optically thin regime, which is unsurprising given the RT problem is almost identical to the gravity problem in the absence of intervening material. That brings up the next part of the algorithm, what to do about tracing a ray in the optically thick regime.

2.2.2 Tracing Rays

In the presence of absorbing material along a ray, the optical depth needs to be computed along said ray by computing the optical depth integral introduced in Eq. 7. To solve this integral numerically, we traverse the tree between the source and resolution element to build up the optical depth. This is

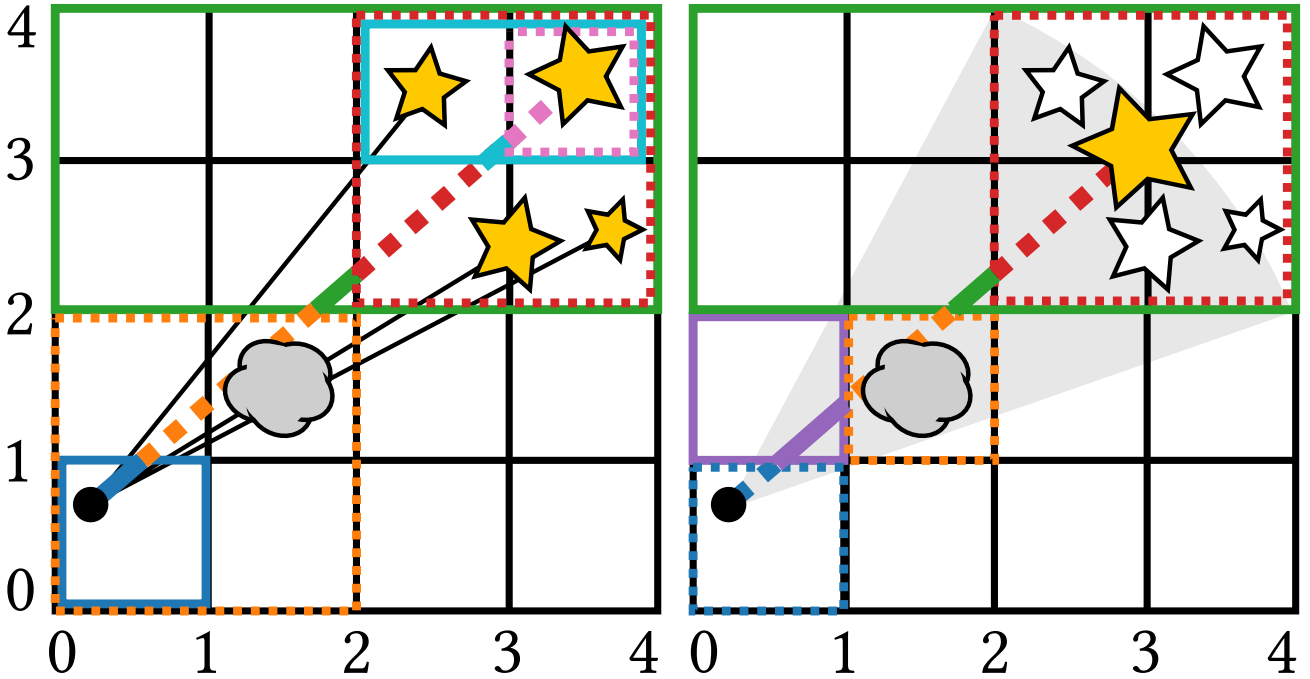


Figure 2.

possible because the tree partitions and fills space, thus all the intervening material should be contained in the tree we traverse. Making use of properties computed during the tree build, we can compute the optical depth of the i 'th piece of the ray (τ_i) using the intersection length of the cell and ray (s_i) as well as the average density ($\bar{\rho}_i$) and average opacity ($\bar{\kappa}_i$) in the cell

$$\tau_i = \bar{\rho}_i \bar{\kappa}_i s_i. \quad (16)$$

The total optical depth is then summed up during the tree walk,

$$\tau = \sum_i \tau_i, \quad (17)$$

giving us everything needed to evaluate Equation 10.

This process is also illustrated in the left panel of Figure 2. In this figure ray segments and corresponding cells share the same colour. When referring to specific cell colours, they will also be identified by two sets of points $[(x, y), (x, y)]$ corresponding to the bottom left and top right vertices of the cell respectively. Dotted lines are used to distinguish consecutive ray segments and help associate ray segments and their corresponding cells. In the left panel of Figure 2 there are two important things to note. Firstly, since we are performing a reverse ray trace, the resolution element denoted by the black circle is intrinsically well resolved at the bucket cell (the blue cell at at $[(0, 0), (1, 1)]$ level). However, the second point is that as the tree is walked upwards space becomes less resolved. It should be apparent that the central parts of the ray are less resolved (the green cell at $[(0, 2), (4, 4)]$) and as you move towards the source or resolution element the ray becomes more resolved (the red cell at $[(2, 2), (4, 4)]$ and the orange cell $[(0, 0), (2, 2)]$). This can be looked at in two ways.

If the medium is uniform, the algorithm can be extremely efficient while still being able to resolve a sharp feature in the radiation field such as an ionization front. However, if the medium is highly irregular along the ray the algorithm will not be able to resolve sharp density and opacity gradients which could significantly alter the optical depth. Thus adaptive refinement is needed during the tree walk to accurately resolve the medium along the ray.

2.2.3 Adaptive Refinement

Consider the right panel in Figure 2. A dense blob of gas to be resolved resides in the orange highlighted cell at $[(1, 1), (2, 2)]$. At the point in the tree walk where we reach the orange highlighted cell at $[(0, 0), (2, 2)]$ in the left panel, a decision needs to be made on whether the current cell sufficiently represents the media. This decision is made by a refinement criteria. If the cell passes the criteria to refine, rather than using its average properties we recursively check the cell's children until the criteria fails. Thus building a better resolved section of the ray.

Difficulty comes in choosing a refinement criteria that is both accurate and efficient. Ideally, the criteria should be true when an average optical depth in a region may not be accurate to the true distribution, such as a clumpy medium where the average density and opacity is much higher than the “effective” density and opacity (Városi & Dwek 1999; Hegmann & Kegel 2003). For this reason we have chosen an optical depth based refinement criteria that is unique to TREVR.

Consider two rays through through a large cell as in Figure 3. These rays represent what the case would be if

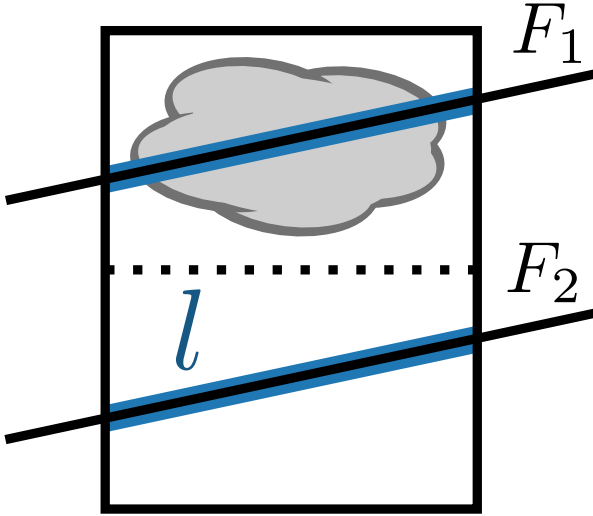


Figure 3.

properties of the children were used instead of the parent cell. We can compute the minimum and maximum absorption coefficients α_{\min} and α_{\max} , via their minimum and maximum density and opacity values computed during the tree build. This multiplied by the intersection length l gives us the minimum and maximum optical depths, τ_{\min} and τ_{\max} . We can then test the following refinement criteria

$$\tau_{\text{ref}} < \tau_{\max} - \tau_{\min}, \quad (18)$$

and refine if it is true. The fractional error in flux, per ray segment, for a chosen value of τ_{ref} is

$$\frac{F_1 - F_2}{F_1} \leq 1 - e^{-\tau_{\max} - \tau_{\min}} \lesssim \tau_{\text{ref}}, \quad (19)$$

for small τ , making the refinement criteria a convenient choice of parameter for controlling error.

If the refinement criteria passes at the bucket level, individual particles within a bucket are considered. A straight forward N^2 ray tracing scheme similar to SPHray (Altay et al. 2008) can be performed on bucket particles and their neighbours. In the worst case where the refinement criteria passes the bucket level every time, a cost of $\mathcal{O}(C_n N)$ is added to the scaling, where C_n is the constant number of SPH neighbours.

Fully characterizing the computational cost of the algorithm including the addition of adaptive refinement follows the same method as used earlier. However, now instead of integrating the number of sources we integrate the total number of ray segments computed. We will look at two cases, not refining at all and fully refining down to the bucket level. This will give us upper and lower bound for the algorithms scaling as characterizing the refinement between these extremes depends on the specific density and opacity distributions being operated on.

First let's consider the case where the refinement criteria always passes and all rays are resolved down to the bucket level. The number of segments per ray is then just the length of a ray divided by the size of a bucket. We can

express this as

$$N_{\text{seg}} = \frac{r}{R_0} = \frac{r}{R} \left(\frac{N}{N_B} \right)^{\frac{1}{3}} \quad (20)$$

after substituting Eq. 13 in for R_0 . Since N_{source} is also the number of rays computed, the total number of ray segments computed is just Eq. 12 multiplied by the number of ray segments

$$N_{\text{seg}} = \int_{\left(\frac{N}{N_B}\right)^{-\frac{1}{3}}}^R \frac{4\pi r^2}{\theta_{\text{open}}^3} \frac{r}{R} \left(\frac{N}{N_B} \right)^{\frac{1}{3}} dr \sim N(2N/N_B)^{\frac{1}{3}}. \quad (21)$$

This results means that the total cost of the algorithm scales like $\mathcal{O}(N^{4/3})$ in the worst case.

In the case where the refinement criteria never passes, the ray is split into segments made up of the cells traversed in the tree walk of the sub-tree going from source to resolution element. The number of cells traversed in a tree walk is equal to the logarithm of the number of leaf nodes contained within the sub-tree. The number of leaf nodes in the sub-tree is also given by Eq. 20, so by taking the logarithm of Eq. 20 and adding two for the two buckets on either side of the sub-tree we come to

$$N_{\text{seg}} = \log_2 \left[\frac{r}{R} \left(\frac{N}{N_B} \right)^{\frac{1}{3}} \right], \quad (22)$$

where the logarithm is base two as GASOLINE and thus TREVR is implemented using a binary tree. As before we multiply Eq. 12 by the number of ray segments and integrate the following

$$N_{\text{seg}} = \int_{\left(\frac{N}{N_B}\right)^{-\frac{1}{3}}}^R \frac{4\pi r^2}{\theta_{\text{open}}^3} \log_2 \left[\frac{r}{R} \left(\frac{N}{N_B} \right)^{\frac{1}{3}} \right] dr \sim N \log^2(128N/N_B). \quad (23)$$

This results means that the total cost of the algorithm scales like $\mathcal{O}(N \log^2 N)$ in the best case.

2.2.4 Background Radiation

In order to treat simulations properly we must account for the radiation coming from the rest of the universe outside of the simulation volume. Most current codes apply a constant UV field to the entire box, essentially the lowest order approximation possible. Some specialized codes like URCHIN (Altay & Theuns 2013) do a reverse ray trace to the edge of the box, where the background flux is assumed to be coming from. Others, such as TRAPHIC (Pawlik & Schaye 2008) allow their ray trace to be periodic. We believe that this periodic treatment is problematic. The cosmic UV radiation field originates from very large distances on the order of a gigaparsec. This is too large of a region to practically simulate, so radiation originating from periodicity is too local.

Instead, we have implemented a method involving tracing “background sources” similar to URCHIN. “Background” particles are distributed in a spiral pattern on the surface of a sphere at the very edge of the simulation volume (or at a large distance if required) and the number of sources can be varied to match the required angular resolution of the background. Finding the flux at the centre of a sphere of sources is a problem akin to Newton’s Shell Theorem. However, because the intensity does not cancel like force, the solution

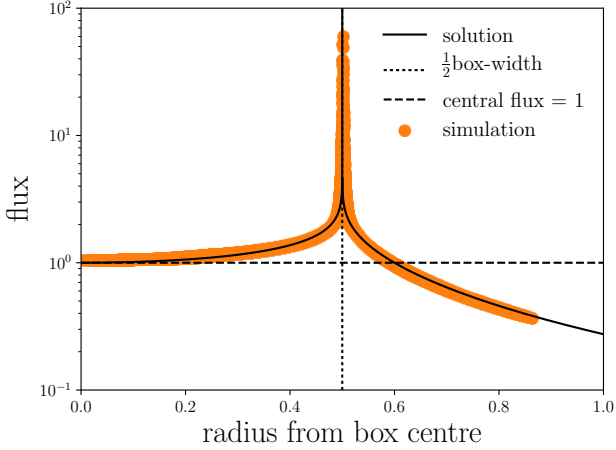


Figure 4.

differs and is as follows:

$$F(r) = \frac{L}{8\pi R} \ln \left(\frac{R+r}{R-r} \right), \quad (24)$$

where L is the total luminosity of the emitting shell, R is the radius of the sphere and r is the radius the flux is being computed at. The shape of the function can be seen in Figure 4 where we have plotted the flux as a function of radius for a homogeneous, optically thin test volume.

Note that due to the logarithm in Equation 24, the flux is nearly constant at small radii. Since most cosmological zoom in simulations only consider gas at a fairly small radius, this setup of background sources is an acceptable method to provide a background flux. A benefit of this method is that we can use all of the existing machinery described in the methods section, and only have to add temporary background star particles as the source of the background radiation. Also note that the simulation flux is over estimated near the central region and underestimated at large radii. When merging background sources which are all located on the surface of a sphere, the merged centre of luminosity will always be at a smaller radius than that of the sphere radius. This can be remedied by enforcing merged background sources to always be located on the sphere.

2.3 Implementation Specifics

As mentioned earlier, TREVR is not specific to either GASOLINE or SPH. However, in this subsection we would like to take the time to go over some implementation specifics.

In the current version of TREVR, a separate tree is built for computing radiative transfer. For development this is a convenient choice, but adds extra cost and in the future a “one tree to rule them all” approach should be adopted. The radiation tree inherits its binary cell splitting from the main tree in Gasoline. One of the main differences between these trees is that the radiation tree is required to fill all space to enable, whereas the main tree “squeezes” cell bounds to the furthest extents of an particle’s influence. This does not work in the context of RT as cell and ray intersections need to be computed to sum up a correct optical depth.

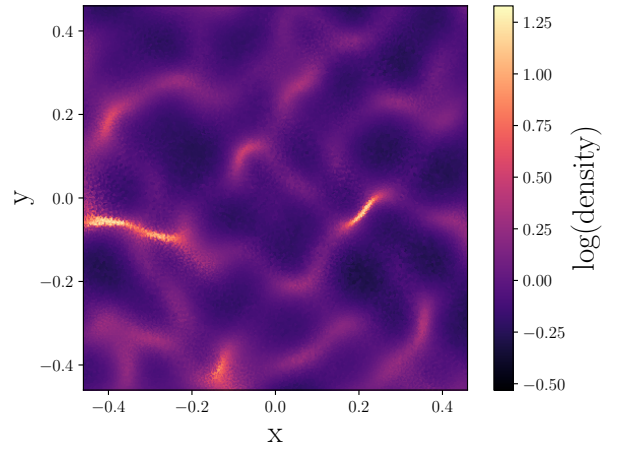


Figure 5.

3 CODE TESTS

3.1 Sinusoidally Perturbed Glass

3.1.1 Initial Conditions

To test the accuracy and general scaling of the algorithm, an varying initial condition (IC) that the accuracy criterion can operate on while being representative of a typical use case is needed. For this we have created a novel IC comprised of a unit length glass of N SPH gas and N star particles whose positions have been perturbed by 24 random sinusoidal modes. The initial glass of particles comes from as 16^3 glass used to create initial conditions for other tests of GASOLINE (Wadsley et al. 2017). The total mass of gas particles is one, and the opacity of each particle is also one. This results in an optical depth across the width of the box of ~ 1 , making the simulation volume optically thin overall with dense, optically thick filamentary structure and underdense voids qualitatively similar to the cosmic web. Each star particle is also assigned a luminosity of one. A slice of this density distribution is plotted in Figure 5. Appendix A contains a detailed explanation of how this IC was created including a table of modes used.

3.1.2 Opening Angle

The opening angle criteria’s affect on accuracy and cost was tested by simulating the optically thin, sinusoidally perturbed glass IC with θ_{open} varying between 0 and 1. The results of this test are plotted in Figure 6. The measure of cost is plotted as the total number of rays, N_{rays} , computed per resolution element on the left y-axis. The number of rays is equivalent to the number of radiation sink-source interactions computed in a simulation time step. Using rays as a measure of cost allows us to separate the affects of the refinement criteria on cost. On the right y-axis, the root mean squared (RMS) fractional error relative to the radiation field computed with $\theta_{\text{open}} = 0$. A refinement criteria value of $\tau_{\text{ref}} = 0.1$ and $N = 64^3$ for both star and gas particles.

At $\theta_{\text{open}} = 0.75$, the value used in all other tests and the

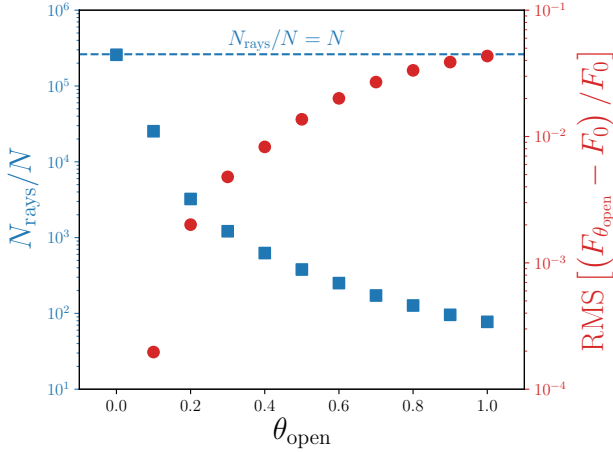


Figure 6.

default value for θ_{open} in many gravity solvers, 200 rays are computed per resolution element with an RMS fractional error of 3%. To get to an RMS fractional error of about 1%, a opening angle of $\theta_{\text{open}} = 0.45$ is needed and costs only 500 rays per resolution element. The cost at $\theta_{\text{open}} = 0.45$ is still much less than interacting with all 64^3 (2.6×10^5) sources, and could be a standard default value to move forward with.

3.1.3 Refinement Criteria

Testing the refinement criteria is similar to testing the opening angle criteria. Again, the sinusoidally perturbed glass IC was simulated but now with a varying τ_{ref} value. The results of this test are plotted in 7. The min and max values of τ_{ref} tested were chosen such that the cost curve flattens out on either side. The left hand side being where refinement has occurred down to the bucket level, and the right hand side end being where refinement is never done. A opening angle of 0.75 was used and $N = 64^3$ for both star and gas particles. Cost is plotted on the left y-axis and RMS fractional error on the right y-axis. The measure of cost is now number of ray segments per resolution element, since the refinement criteria controls how refined a ray becomes. The measure of accuracy is again the RMS fractional error, but now relative to the radiation field computed with $\tau_{\text{ref}} = 1 \times 10^{-8}$, the lowest τ_{ref} tested.

At $\tau_{\text{ref}} = 0.1$, 1% RMS fractional error is achieved with a cost of approximately 850 ray segments computed per resolution element, less than half the cost of refining all the way to the bucket level. Note also that RMS fractional error as a function of τ_{ref} behaves predictably, lying below the $\text{RMS} = \tau_{\text{ref}}$ line and roughly following the $\text{RMS} = \tau_{\text{ref}}/10$ line plotted in Figure 7. This is in agreement with our theoretical claim in Equation 19, that the maximum allowable error in flux per ray segment should be less than and proportional to τ_{ref} for small τ .

The RMS fractional error maxes out at 2-3% in this test. In this particular implementation of TREVR, the walk along the ray goes up from both the bucket where the radiation sink resides and the opened cell where the source resides to the top of the tree. This built in level of refinement is the

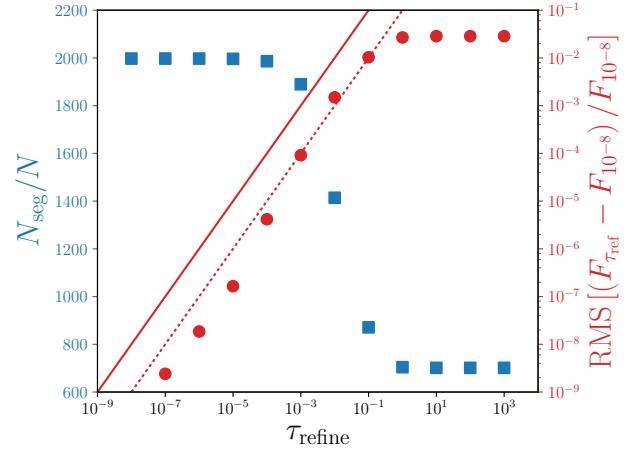


Figure 7.

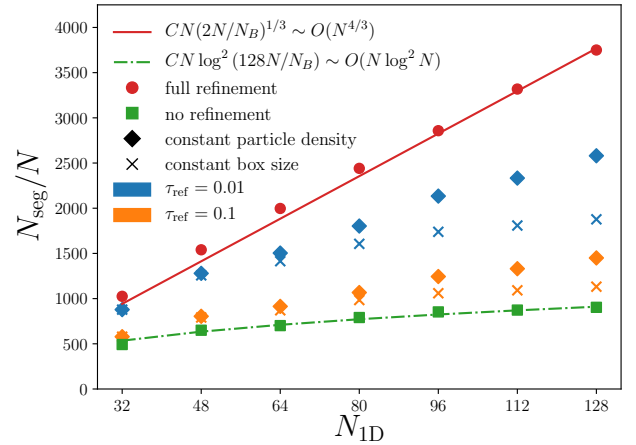


Figure 8.

reason for the low maximum error. Other implementations, that walk the ray top down or up and then back down the tree, would need to rely more or solely on the refinement criteria. In principle, such a method could perform better than $O(N \log^2 N)$.

3.1.4 Scaling

To test cost scaling as a function of N , we hold θ_{open} constant at 0.75 and vary N between 32^3 and 128^3 in steps of $N_{\text{ID}} = 16$ for both gas and star particles. To substantiate our best and worst case theoretical scaling claims made in Equations 23 and 21 respectively, the sinusoidally perturbed glass IC was simulated with $\tau_{\text{ref}} = 1 \times 10^6$ to insure refinement was never performed and with $\tau_{\text{ref}} = 0$ to insure refinement was always performed down to the bucket level. Data from these tests and fitted theoretical lines were plotted in Figure 8 and correspond very closely to each other. Note that the only parameter used to fit the theoretical lines from was a constant factor of C placed in front of Equations 21 and 23.

Scaling behavior between the upper and lower limits was probed in two ways. Firstly, simulations were run with τ_{ref} values of 0.1 and 0.01. Secondly, strong and weak scaling cases were simulated. The strong scaling case being where the box size was held constant and particle number increased. This is analogous to increasing the resolution of an isolated galaxy simulation. The weak scaling case is the opposite, where the box size is increased and particle density is held constant. This is analogous to simulating larger and larger cosmological boxes to achieve larger statistical samples.

Again, data from these tests was plotted in Figure 8 where there are two interesting things to note. Firstly, the strong scaling case, which is typically the harder case to scale well in, scales better than the weak scaling case. The strong scaling data turns over more similarly to the $N \log^2 N$ function and costs less than the weak scaling data. This is because unlike gravity, tracing a ray through intervening material will always cost more on longer length scales. Whereas in the strong scaling case, an increased number of particles represent the same density and opacity distribution and the refinement criteria will still act in the similar way, now with more particles per cell to average over. The second thing to note is that the strong scaling case at $\tau_{\text{ref}} = 0.1$, which achieved an RMS fractional error of 1% in the $N = 64^3$ sinusoidally perturbed glass test, scales similarly to the no refinement data and fit to $N \log^2 N$.

3.2 Isothermal Spheres

3.2.1 Initial Conditions

The sinusoidally perturbed glass IC tested a generally optically thin, smooth density distribution. This is a good proxy for many astrophysical cases of interest, such as late stage galaxy evolution. As a test of how TREVR's refinement criteria can handle compact, optically thick features we created the Isothermal Spheres IC. This IC consists a single radiation source positioned in the top left corner and four spheres with $1/r^2$ density profiles embedded in a uniform glass. The spheres produce shadows down and to the right of the source. Accurate shadows can only be cast if the sharply peaked spheres are resolved correctly by the refinement criteria. Error specifically in the optically thick regime can be separated out by looking at only particles in shadow. The four isothermal spheres follow the density distribution described by

$$\rho(r) = \frac{\rho_0 \epsilon}{r^2 + \epsilon^2}, \quad (25)$$

where the softening length, ϵ , is 0.002 and the central density, ρ_0 , is 626. The IC was made by adding SPH gas particles near the sphere centers using a stretched glass of. **Grond: James, could you fill this part in? I don't have the script you used to do this on hand.** These parameters set the maximum optical depth through a sphere to $\tau_{\text{max}} = 4$ (98% reduction in flux) and the density at the edge of the spheres to one, matching the unit density of the uniform background. The isothermal spheres have a radius of 0.05 and are denoted by the grey circles in Figure 9. They are centred on the x and z axis with y coordinates given by

$$y_i = 0.75 - 1.3^{-(4-i)}, \quad (26)$$

where i runs from zero to three. The radiation source, denoted by the black star in Figure 9, is located at $x = 0.49$, $y = y_0$ and $z = 0$. The total number of particles in the IC is $N = 4111624$.

3.2.2 Refinement Criteria

The effects of the refinement criteria on accuracy and cost in this test were analyzed similarly to the data plotted for the Sinusoidally Perturbed glass IC test in Figure 7. The main addition to Figure 10 is the subset of particles in shadow has its RMS fractional error plotted separately to probe the refinement criteria's performance in the optically thick regime. Again, $\tau_{\text{ref}} = 0.1$ achieves an RMS fractional error of 1% with very little cost. However, when only considering particles in shadow the same refinement criteria produces almost an order of magnitude more error at about 8%. Decreasing the refinement criteria by an order of magnitude to $\tau_{\text{ref}} = 0.01$ predictably decreases the RMS fractional error on particles in shadow to 1% with a negligible cost increase from $\tau_{\text{ref}} = 0.1$.

The $\text{RMS} = \tau_{\text{ref}}$ and $\text{RMS} = \tau_{\text{ref}}/10$ lines are again plotted in Figure 10. For the most part the RMS fractional error is contained between these lines, with only two of the in-shadow points at $\tau_{\text{ref}} = 1 \times 10^{-5}$ and 1×10^{-4} , and one of the all particle points at $\tau_{\text{ref}} = 1 \times 10^{-4}$ sitting ever so slightly above the $\text{RMS} = \tau_{\text{ref}}$ line. Again, but now in a more difficult test when compared to the sinusoidally perturbed glass IC, Equation 19 proves to accurate in predicting that the maximum allowable error in flux per ray segment should be less than and proportional to τ_{ref} despite only technically being valid for small τ . In most cases we believe TREVR should perform better as Equation 19 is just a reliable upper bound.

Wadsley: What about work we did for absolute errors? I'd like at least a comment with quantitative error numbers and preferably a plot too. Grond: I'll make this for my thesis ASAP and put it here after.

3.3 Strömgren Sphere Test

3.3.1 Strömgren Sphere Theory

The Strömgren sphere is a theoretical ionized sphere of gas first discussed by Bengt Strömgren in 1938 (Strömgren 1939) as a model of regions around hot, young stars. The theoretical initial conditions consist of a cloud neutral hydrogen gas with an ionizing source of radiation at its centre. As photons from the source ionize the hydrogen, the optical depth of the gas decreases and so the ionizing photons are able to travel further and further from the source creating an ionization front. As the front moves radially outward from the source a radius is reached where the ionization rate equals the recombination rate. At this point, the front reaches equilibrium and stops creating a stable sphere of ionized hydrogen. The Strömgren sphere test has become a common code test in RT methods papers (Pawlik & Schaye 2008, 2011; Petkova & Springel 2011) and comparison papers (Iliev et al. 2006, 2009), as it is a simple test of a method's ability to resolve ionization fronts and achieve equilibrium behaviour.

The equilibrium radius or Strömgren radius, R_S , is the radius at which the ionization and recombination rates are

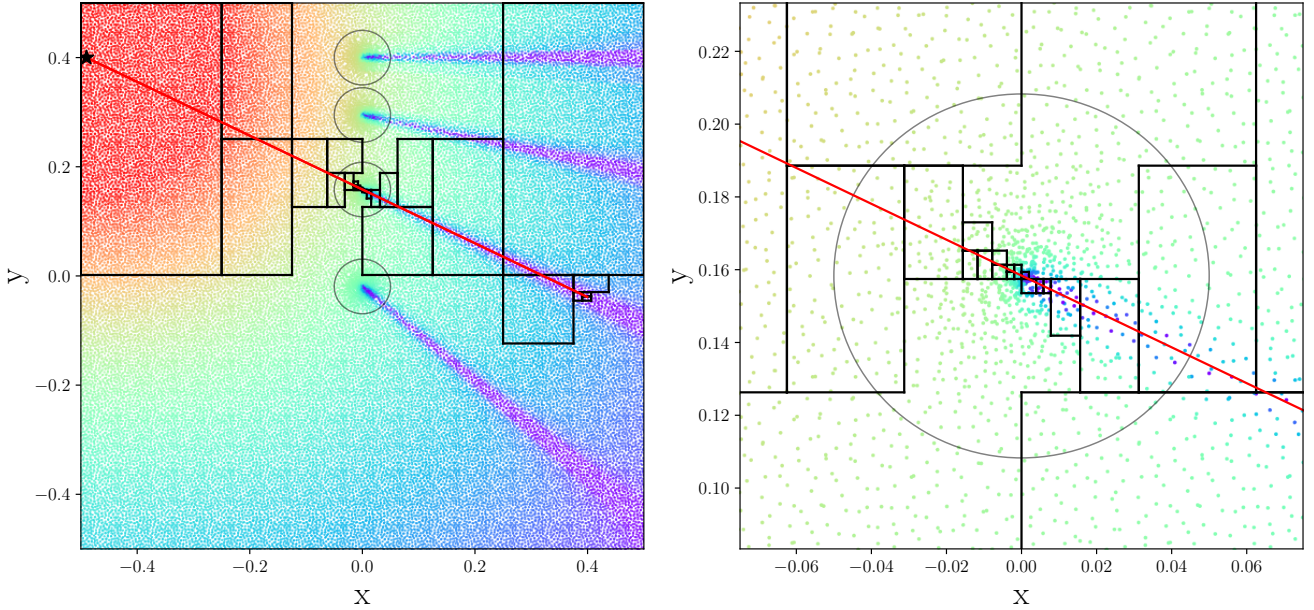


Figure 9.

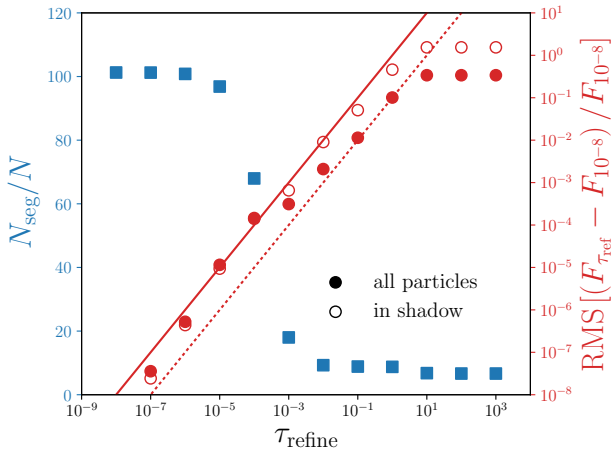


Figure 10.

equal. This radius can be solved for by setting the two rates equal producing (e.g. Tielens 2005)

$$R_S = \left(\frac{3}{4\pi} \frac{\dot{N}_\gamma}{\alpha n_H^2} \right)^{1/3}, \quad (27)$$

where \dot{N}_γ is the source luminosity in photons per second, α is the recombination rate and n_H^2 is the hydrogen number density. One can also solve for the radius as a function of time (e.g. Spitzer 1978),

$$R(t) = R_S [1 - \exp(t/t_{\text{rec}})]^{1/3} \quad (28)$$

where $t_{\text{rec}} = 1/n_H \alpha$ is the recombination time of the gas. The above derivation assumes a “sharp” ionization front, meaning the transition from ionized to neutral hydrogen is across

an infinitesimally small region. In practice, the transition region is small compared to the size of the ionized region, but there is structure interior to the Strömgen radius that is not accounted for by simply solving for the equilibrium radius. In order to solve for the non-sharp ionization front we must consider the hydrogen ionization equation

$$\frac{\partial n_{\text{HII}}}{\partial t} = c\sigma n_{\text{HI}} n_\gamma - \alpha n_e n_{\text{HII}}, \quad (29)$$

where n_x is the number density of species x , HI and HII are neutral and ionized hydrogen respectively, γ is photons, σ is the ionization cross section, c is the speed of light and α is the recombination rate. Note that we have omitted collisional ionization in Equation 29 as it is not included in further testing, however it should be included in general. By integrating the ionization equation and the flux equation with absorption (Equation 10), we get a solution for HI/HII as a function of radius and as a function of time (Osterbrock & Ferland 2006). In the following tests, we include both theoretical sharp front solution and non-sharp front solutions from the Iliev et al. (2006) comparison paper to compare to our results as well as mimicking their initial conditions.

3.3.2 The Isothermal Strömgen Sphere

In the simplest case, the ionizing source is assumed to emit monochromatic photons at 13.6 eV, meaning the gas is ionized but not heated. The gas is not allowed to cool, meaning the gas is isothermal. For this reason we will refer to this case as the Isothermal Strömgen Sphere. The medium is initially neutral with a temperature of $T = 10^4$ K and a density of $n_{\text{HI}} = 10^{-3} \text{ cm}^{-3}$. An ionizing source is turned on at $t = 0$ and emits at a rate of $\dot{N}_\gamma = 5 \times 10^{48} \text{ photons s}^{-1}$. We use an ionization cross section of $\sigma = 6.3 \times 10^{-18} \text{ cm}^2$ and a recombination rate of $\alpha = 2.59 \times 10^{-13} \text{ cm}^3 \text{ s}^{-1}$, typical of 10^4

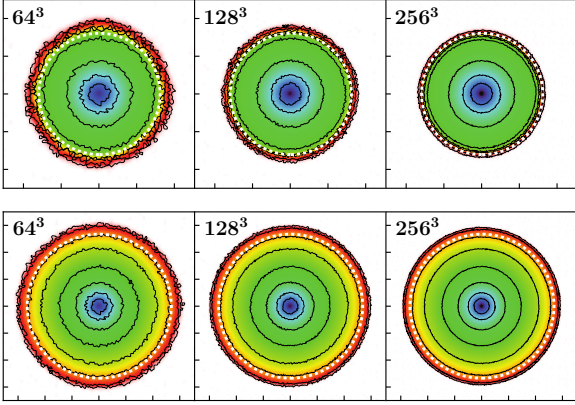


Figure 11.

K gas. These values yield a Strömgren radius of $R_S = 5.38$ kpc and a recombination time of $t_{rec} \approx 125$ Myr.

We note that [Iliev et al. \(2006\)](#) uses a 6.6 kpc cube which only contains a single quadrant of the Strömgren sphere for their testing. We have opted to use an 16 kpc cube, increasing the maximum front radius to 8 kpc to avoid any edge effects, as the sphere gets close to the edge of the box for some codes in their paper. In order to aid comparison, we still normalize radius values to 6.6 kpc, as is done in [Iliev et al. \(2006\)](#). As well, we have not imposed a floor on the HII fraction of 0.001, as has been done in their paper. As the resolution used in the [Iliev et al. \(2006\)](#) comparison paper was never specifically given, we have opted to run the test with $N = 64^3$, 128^3 and 256^3 particles to represent the *entire* sphere. These resolutions correspond to single quadrant resolutions of $N = 32^3$, 64^3 and 128^3 in [Iliev et al. \(2006\)](#). Varying the number of particles also allows us to have a look at how TREVR converges with resolution. We have run our Strömgren sphere tests with fixed accuracy parameters of $\theta_{open} = 0.75$, $\tau_{ref} = 0.1$.

Figure 11 is a slice through the z -plane of the simulation. The colour map corresponds to neutral fraction. The contour levels and colour map have been chosen to closely mimic Figure 6 in both [Pawlik & Schaye \(2008\)](#) and [Pawlik & Schaye \(2011\)](#). We have done this to highlight a main benefit ray tracers like TREVR have over photon packet propagation methods such as TRAPHIC - isotropy. At the same $N = 64^3$ particle resolution TREVR is more isotropically symmetric than TRAPHIC, even with their use of monte-carlo resampling. Furthermore, TREVR outperforms TRAPHIC in this aspect even at early times (top panels in Figure 11). Here the interior of the Strömgren sphere is represented by 3.3 times fewer particles than late time spheres in equilibrium plotted in the TRAPHIC papers (in this paper these are in the top panels of Figure 11).

Figure 12 is a plot of neutral/ionization fraction as a function radius from the Strömgren sphere centre. The sharp Strömgren radius is plotted as well as non-sharp solutions from all codes presented in Figure 8 of [Iliev et al. \(2006\)](#). TREVR tends to over-ionize at lower resolutions, but recreates the ionization profile quite well overall. At 30 Myr we converge with resolution to the sharp solution. At 500 Myr we converge to the non-sharp numerical solutions, which also

over-ionize relative to the sharp solution at late times. Overall, the two higher resolution solutions are within the scatter of the non-sharp solutions of the codes presented in [Iliev et al. \(2006\)](#). It is interesting to not that the magnitude of over-ionization is related to resolution. We suspect the cause of over-ionization is **Grond: What exactly do we want to say here?**.

3.3.3 The Non-Isothermal Strömgren Sphere

The above test assumed the hydrogen gas was isothermal and that all incident photons had the same energy. In reality, photons range across many wavelengths with differing cross-sections at each wavelength. As well, absorption typically causes heating, which effects among many gas properties, recombination rate.

We rerun the Strömgren sphere test, but this time the incident photons are assumed to be from a black body with temperature 10^5 K. The cross section is now an integrated cross section, obtained by integrating the cross section as a function of wavelength between 13.6 eV and 29.65 eV, which gives $\sigma = 1.63 \times 10^{-18} \text{ cm}^{-2}$. The gas has an initial temperature of 100 K and the recombination rate is a function of temperature set by

$$\alpha(T) = 2.59 \times 10^{-13} \left(\frac{T}{10^4 \text{ K}} \right)^{-0.7} \text{ cm}^{-3} \text{ s}^{-1} \quad (30)$$

to match [Petkova & Springel \(2009\)](#). This test includes heating due to absorption and cooling due to recombination Δ_r , collisional ionization Δ_{ci} , line cooling δ_l and Bremsstrahlung radiation Δ_B . The rates are taken from [Cen \(1992\)](#) in order to match [Petkova & Springel \(2009\)](#).

Figures 13 and 14 show the neutral/ionized fraction and temperature respectively as a function of radius at $t = 10$, 100 and 500 Myr. These times represent the fast expansion stage, slowing down stage and final Strömgren sphere respectively. We have plotted numerical solutions from Figures 16 and 17 in [Iliev et al. \(2006\)](#) for comparison. Again, TREVR recreates these profiles quite well in a qualitative sense. However, TREVR over-ionizes relative to all other solutions at every resolution. We believe this is not caused by the TREVR algorithm specifically, as the isothermal test converged with resolution. It could possibly be a result of the ionization code and should be addressed in the future **Grond: Again, exactly what do we want to say here?**. On the other hand, the temperature profile lies in the middle of the scatter of the [Iliev et al. \(2006\)](#) solutions.

4 DISCUSSION AND CONCLUSIONS

Best practices

- what parameters do we suggest based on testing? What one should be careful about.
- specific things we will do wrong?

now we have this we can do these things

Our Niche

- why are isolated galaxy simulations best right now
- use in small scale, low source stuff?
- reionization is bad

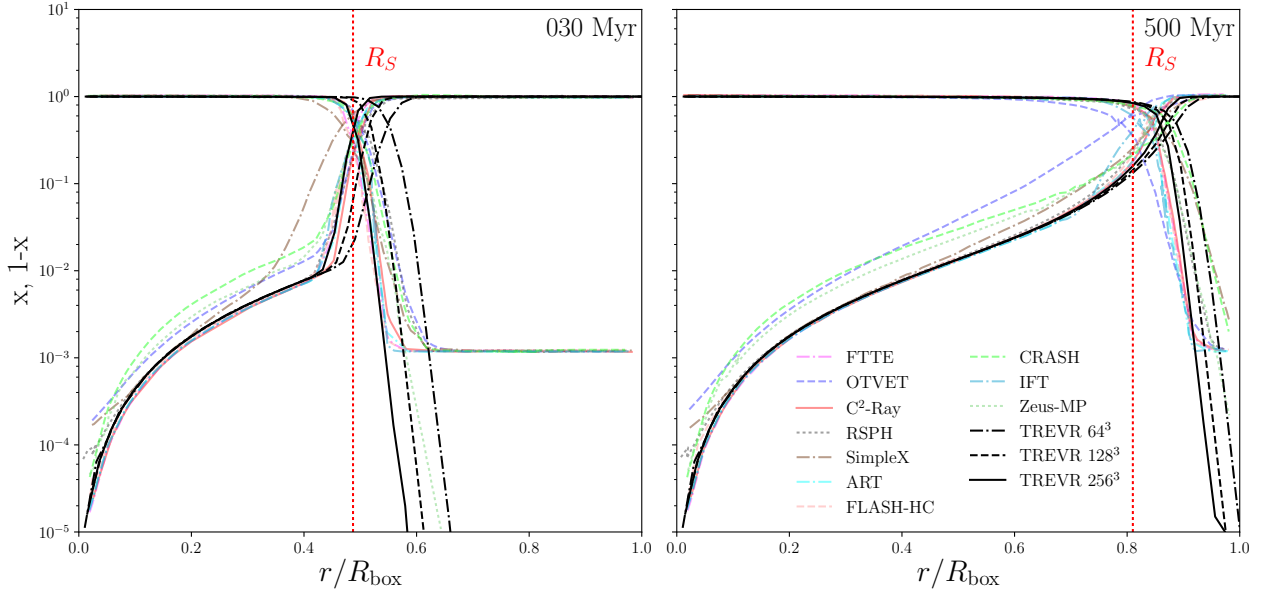


Figure 12.

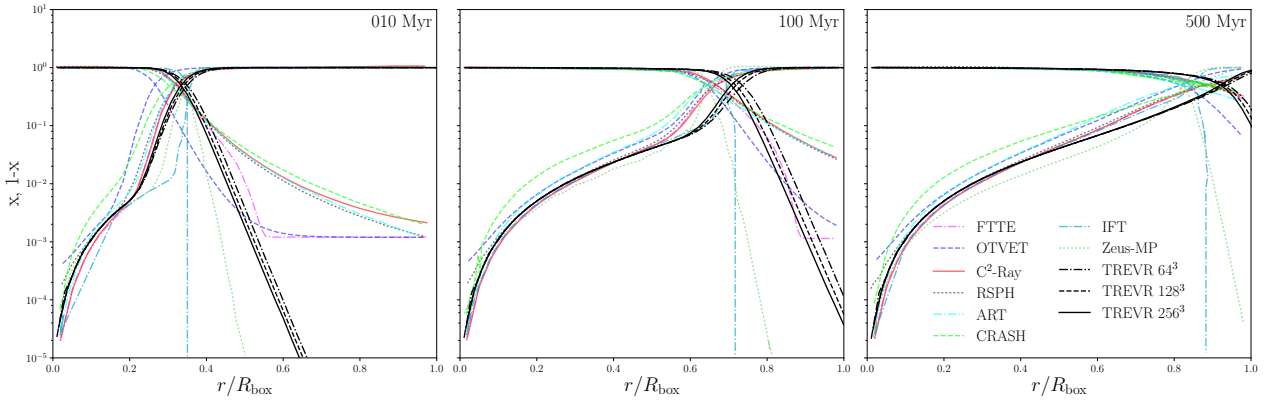


Figure 13.

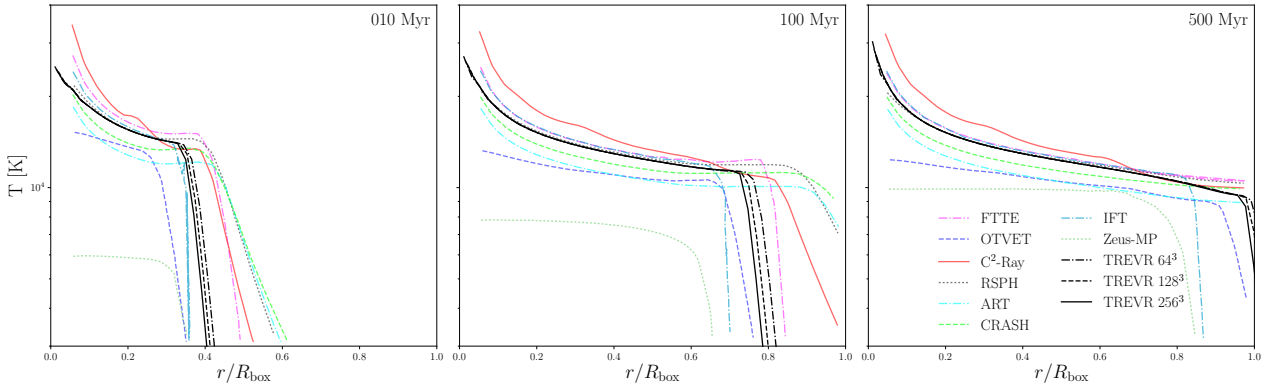


Figure 14.

- challenges for the cosmological box use case

Future Work

- How to deal with periodicity
- How to deal with finite speed of light (look back)
- More optimizations (turning off sources, when to stop tracing a ray)
- Complex source problem, why it might not be so bad

General Wrap Up

- Hammer out main points we want to end on (maybe in a list)

strict time step

- problem with cosmology (regions of space that generate UV field are enormous Gpc, add in background by hand)
- scaling stuff is not specific to gasoline NB=1 - pp (explain it more in context of gasoline) - cosmo background (stuff merged on sphere)

32*3*N (more hops, resampling)

gasoline has multiple trees (3 trees), future work -> one tree to rule them factor of 3

int gasoline section (like sph ray?? how exactly)

For discussion should talk about how this (iso spheres) is hard test – single source. In more general case if goal is radiation field for chemistry or similar errors will tend to cancel in rms

Discussion: Traffic

~32 (N+Nvip) packets - 64 N packet hops per substep – often more even with reduced speed of light b/c must cover $c \times dt$ (I think Rahmati gave large multiplier) Will be of order $c_{\text{light}}/c_{\text{sound}}$ Can't really win by doing fewer RT step since just increases the substep required $U_s \sim 1000 N_{\text{sink-active}}$
~10 N per substep, no subcycling needed because on average $N_{\text{sink-active}} \sim 1/100 N$

Discussion should include possible future improvements
Note: Healpix doesn't change order! $6N \rightarrow N$

ACKNOWLEDGEMENTS

REFERENCES

- Altay G., Theuns T., 2013, *MNRAS*, **434**, 748
Altay G., Croft R. A. C., Pelupessy I., 2008, *MNRAS*, **386**, 1931
Baczynski C., Glover S. C. O., Klessen R. S., 2015, *MNRAS*, **454**, 380
Barnes J., Hut P., 1986, *Nature*, **324**, 446
Benz W., 1988, *Computer Physics Communications*, **48**, 97
Cen R., 1992, *ApJS*, **78**, 341
Chabrier G., 2003, *PASP*, **115**, 763
Clark P. C., Glover S. C. O., Klessen R. S., 2012, *MNRAS*, **420**, 745
Dale J. E., Ercolano B., Bonnell I. A., 2012, *MNRAS*, **424**, 377
Gnedin N. Y., Abel T., 2001, *New Astron.*, **6**, 437
Gritschneider M., Naab T., Walch S., Burkert A., Heitsch F., 2009, *ApJ*, **694**, L26
Hegmann M., Kegel W. H., 2003, *MNRAS*, **342**, 453
Howard C. S., Pudritz R. E., Harris W. E., 2016, *MNRAS*, **461**, 2953
Howard C. S., Pudritz R. E., Harris W. E., 2017, *MNRAS*, **470**, 3346
Hubber D. A., Batty C. P., McLeod A., Whitworth A. P., 2011, *A&A*, **529**, A27
Iliev I. T., et al., 2006, *MNRAS*, **371**, 1057

- Iliev I. T., et al., 2009, *MNRAS*, **400**, 1283
Kannan R., et al., 2014, *MNRAS*, **437**, 2882
Leitherer C., et al., 1999, *ApJS*, **123**, 3
Mellema G., Iliev I. T., Alvarez M. A., Shapiro P. R., 2006, *New Astron.*, **11**, 374
Mihalas D., Mihalas B. W., 1984, Foundations of radiation hydrodynamics. Courier Corporation
Osterbrock D. E., Ferland G. J., 2006, Astrophysics of gaseous nebulae and active galactic nuclei
Paardekooper J.-P., Kruip C. J. H., Icke V., 2010, *A&A*, **515**, A79
Pawlik A. H., Schaye J., 2008, *MNRAS*, **389**, 651
Pawlik A. H., Schaye J., 2011, *MNRAS*, **412**, 1943
Petkova M., Springel V., 2009, *MNRAS*, **396**, 1383
Petkova M., Springel V., 2011, *MNRAS*, **415**, 3731
Rosdahl J., Teyssier R., 2015, *MNRAS*, **449**, 4380
Spitzer L., 1978, Physical processes in the interstellar medium
Springel V., Yoshida N., White S. D. M., 2001, *New Astron.*, **6**, 79
Strömgren B., 1939, *ApJ*, **89**, 526
Tielens A. G. G. M., 2005, The Physics and Chemistry of the Interstellar Medium
Városi F., Dwek E., 1999, *ApJ*, **523**, 265
Vine S., Sigurdsson S., 1998, *MNRAS*, **295**, 475
Wadsley J. W., Stadel J., Quinn T., 2004, *New Astron.*, **9**, 137
Wadsley J. W., Keller B. W., Quinn T. R., 2017, *MNRAS*, **471**, 2357
Walch S. K., Whitworth A. P., Bisbas T., Wünsch R., Hubber D., 2012, *MNRAS*, **427**, 625
Wise J. H., Abel T., 2011, *MNRAS*, **414**, 3458

APPENDIX A: TEST INITIAL CONDITIONS

A1 Sinusoidally Perturbed Glass

To create our gently varying density distribution for the sink/source scaling tests, we modify positions of particles in a glass initial condition by adding the sum of 24 sinusoidal modes as in equation A1 below

$$\vec{r} = \vec{r}_0 + \sum_{i=1}^{24} \frac{1}{275} \sin(k_{x,i} r_x + k_{y,i} r_y + k_{z,i} r_z + \phi_i), \quad (\text{A1})$$

where \vec{r}_0 is the particles initial position in the glass and \vec{r} is its perturbed position in the final distribution. The \vec{k}_i and ϕ_i values are listed in table A1 for if one wishes to reproduce the scaling tests. Both gas and star particles have the same density distribution. However, the initial glass was flipped for the star particles by reassigning x, y and z coordinates via

$$x_{\text{star}} = y_{\text{gas}}, \quad y_{\text{star}} = z_{\text{gas}}, \quad z_{\text{star}} = x_{\text{gas}}, \quad (\text{A2})$$

to prevent the particles from occupying the same position in space.

This paper has been typeset from a \TeX /L \AT\TeX file prepared by the author.

Table A1. Randomly generated \vec{k} and ϕ values used in generating a gently varying density distribution.

i	$k_{x,i}$	$k_{y,i}$	$k_{z,i}$	ϕ_i
01	-3.918398	+1.727743	-4.476095	0.829776
02	-3.681821	-4.619688	+4.865007	3.891157
03	-4.831801	+3.769470	+0.567451	3.668730
04	-2.298279	+1.501757	+4.716946	1.528348
05	-0.289974	-3.097958	+1.270028	4.113001
06	+1.262943	-1.661726	-2.600413	4.481799
07	+1.588224	+4.072259	+0.616444	2.971965
08	-2.253394	-2.806478	+2.749155	0.442241
09	-1.432569	+3.324710	+4.842991	2.871989
10	+1.287742	-4.575517	-4.001723	1.727810
11	+4.769704	+0.540096	-4.203839	5.872117
12	-3.013200	-1.871251	-2.514416	1.574008
13	-4.588620	+4.384224	+1.246849	1.985715
14	-0.372817	+0.195243	+4.074056	6.248739
15	-1.842232	+0.901598	-4.453613	6.273336
16	+1.986937	-1.037650	+1.958888	2.177783
17	-1.748485	-1.386029	+3.755833	0.532604
18	+4.852406	-3.272506	+0.826504	5.525470
19	+3.663293	-4.597598	-0.890135	4.528870
20	-1.720903	+2.726011	+3.192427	3.875610
21	+4.973332	+4.777182	-2.515792	0.406737
22	+0.057238	-2.972427	-1.828550	4.125258
23	+0.938234	-0.487023	-2.755097	1.335299
24	+1.943361	+0.388178	-3.783953	4.774938